Ocean Engineering 254 (2022) 111299

Contents lists available at ScienceDirect

Ocean Engineering

journal homepage: www.elsevier.com/locate/oceaneng

Physics-informed turbulence intensity infusion: A new hybrid approach for marine current turbine rotor blade fault detection

Brittny Freeman[1], Yufei Tang [*,1], Yu Huang[1], James VanZwieten [*,2]

Florida Atlantic University, 777 Glades Road, Boca Raton, FL 33431, USA

ARTICLE INFO

Keywords:
Ocean current turbine
Blade fault detection
Non-intrusive techniques
Machine learning
Physics-informed

ABSTRACT

Ocean current turbines (OCT) convert the kinetic energy housed within the earth's ocean currents into electricity. However, OCT technologies used to harvest this energy are still at an early stage in development due to technical and economic challenges stemming from the high operation and maintenance costs associated with limited geographical location access and harsh operating environments. In an effort to alleviate reliability concerns associated with marine electricity generation, this paper proposes a novel physics-guided rotor blade imbalance fault detection framework that combines non-intrusively acquired fault features obtained from the turbine's electrical power signal with environmental condition data to enhance the fault detection capabilities. The combination of these two data sources paved the way for the development of a physics-informed neural network that ensures the classifications made by our framework are scientifically consistent with the underlining hydro-kinematic rotor dynamics of the OCT. The effectiveness of our framework is validated on simulation data produced by an in-house high-fidelity numerical simulation platform that includes temporally and spatially dynamic oceanic operating environment models. Test results demonstrate a Type-I error rate of 5.00% and a Type-II error rate of 2.92%.

1. Introduction

The kinetic energy within ocean currents, tides, and waves represents a highly concentrated source of clean and renewable energy. However, harsh operating conditions reduces the longevity and reliability of devices designed to extract this energy, and leads to high Levelized Cost of Energy (LCOE). According to Neary et al. (2014), an estimated 26%–32% of the LCOE associated with ocean current turbine (OCT) operation is attributed to O&M costs alone. Additionally, when compared to wind turbines (WT), OCT rotor blade failures are especially pronounce since biofouling issues are prevalent and because sea water is both more corrosive and dense than air.

Fault detection frameworks based on electrical signal analysis are emerging to address rotor blade imbalance fault issues, as they allow for non-intrusive condition-based monitoring to be performed. These techniques customarily investigate the shaft rotating frequency (1P frequency) of the turbine for abnormalities. In Saidi et al. (2020), a framework was developed that employed a bispectrum-based signal processing methodology to analyze the stator current signals acquired from an OCTs suffering from biofouling issues. This bispectrum-based framework achieved better fault detecting success than other Fourier-based signal processing approaches by investigating higher-order statistical dependencies present within the frequency spectra of the generator stator current signals. In Li et al. (2020b), statistical thresholding was used on fault features extracted from OCT stator current signals for rotor blade imbalance fault detection. This method utilized the Hilbert transform and principle component analysis for signal demodulation and feature extraction. Experimental results from this work yielded a Type II error rate of 4.60%, while the Type I error rate was 0.80%. One limitation within both works is that the experiments were performed in a test flume setup that held the rotor rotational speed approximately constant. This implies that these works may be more suitable for fixed speed rotor analysis, as opposed to variable speed.

More recently, it has been found that signal processing and statistical-based fault detection frameworks perform better when their features are utilized by machine learning algorithms. In general, frameworks that incorporate machine learning are better at identifying salient trends masked by frequency smearing and the low signal to noise ratios of electrical signals obtained from the turbine's generator,

* Corresponding authors.
E-mail addresses: bfreem10@fau.edu (B. Freeman), tangy@fau.edu (Y. Tang), yhwang2018@fau.edu (Y. Huang), jvanzwi@fau.edu (J. VanZwieten).
[1] B. Freeman, Y. Tang, and Y. Huang are with the Department of Electrical Engineering and Computer Science, Florida Atlantic University, Boca Raton, FL, 33431, USA.
[2] J. VanZwieten is with the Department of Civil, Environmental, and Geomatics Engineering, Florida Atlantic University, Boca Raton, FL 33431, USA.

https://doi.org/10.1016/j.oceaneng.2022.111299
Received 7 November 2021; Received in revised form 22 March 2022; Accepted 8 April 2022
Available online 29 April 2022

than frameworks that strictly employ signal processing and statistical-based fault detection alone. In Wei et al. (2021), the Hilbert transform and variational mode decomposition were combined with screening linear discriminant analysis to perform rotor blade imbalance fault detection on OCTs operating in a fluctuating current velocity conditions. This framework attained a classification accuracy of 92.04%. In Freeman et al. (2021), Morlet wavelets analysis was used for fault feature engineering and a K-nearest neighbor machine learning algorithm to detect rotor blade imbalance faults. Results from this work indicated an overall 97.78% accuracy score. Neither of these approaches however, adequately assessed how dynamically changing other oceanic environmental parameters, in addition to the flow speed, would affect the classification performance.

Building upon the success garnered from the incorporation of machine learning into signal processing and statistical-based fault detection, a new paradigm of thought has begun traversing throughout the machine learning research community. This line of thought attests that data driven machine learning methodologies, as mentioned previously, can be improved by incorporating scientific prior knowledge into learning pipelines (von Rueden et al., 2019; Karpatne et al., 2017; Rai and Sahu, 2020). In such frameworks, a hybrid combination of training data and preexisting physics knowledge can be combined to ensure the framework learns in a way that respects the underlining physics of the system being studied. The research performed in this work is an extension of the research performed in Freeman et al. (2021), employing a similar physics-informed hybrid approach. In our framework, data simulated by a high fidelity numerical simulation platform (VanZwieten et al., 2013) and prior knowledge related to the spatiotemporal operating environment of the ocean current (i.e., South Florida Gulf Stream) is utilized to develop a novel rotor blade imbalance fault and severity classification framework. From the development of this hybrid framework the following scientific merits are achieved:

1. Our framework integrates prior physics knowledge into the learning pipeline of a neural network. This integration is preformed via the inclusion of a physics-based loss function that alleviates inconsistent target labeling. Specifically, the neural network's loss function is customized to ensure that model predictions are scientifically consistent with the known physics of the turbine's underlining rotor dynamics. Such alleviations are not possible when purely data driven methods are employed for fault detection alone.
2. The incorporation of prior knowledge relating to the oceanic environmental conditions (i.e., current flow velocity, current shear, and turbulence intensity) allows for extensive experimental investigations on the effects these parameters have on the signal morphology of generator power signals, and by extension, rotor blade imbalance faults. From these investigations, we were able to engineer a never before used feature for rotor blade imbalance fault detection. To our knowledge both the detailed morphology investigation and use of the newly engineered feature have not yet been performed in rotor blade imbalance fault detection research.

The remainder of this paper is structured as follows: Section 2 describes the nature of rotor blade pitch imbalance faults and the ways in which oceanic environmental conditions impact generator power signal morphology. Section 3 describes how physics-informed machine learning is integrated into our proposed framework. Section 4 briefly introduces our numerical simulation platform and the environmental parameter case study that we developed to test the robustness of the framework. Section 5 discusses experimental design, quantified results, and provides a comparative study with other state of the art methods in this field. Lastly, Section 6 presents conclusion and ideas for future work. Note that a list of the most relevant parameters used in this paper is shown in Table A.4 in the Appendix.

2. Analysis of rotor blade pitch imbalance faults

Rotor blade pitch imbalance faults occur when the alignment of a rotor blade deviates with respect to the others. In such cases, the shaft drag and torque generated by the misaligned blade will differ from the torque that is generated from the healthy blades. These shaft torque variations generate dynamic loads and vibrations that propagate internally throughout the turbine via the electromechanical coupling that exists between the rotor shaft and generator (Gong and Qiao, 2012).

The equation of motion of a direct drive OCT turbine rotor can be expressed similarly to Gong and Qiao (2012) and Zhang et al. (2017) as:

$$J_{\mathcal{R}} \cdot \frac{d\omega_{\mathcal{R}}}{dt} = T_{\mathcal{R}} - T_{\mathcal{E}} \tag{1}$$

where $J_{\mathcal{R}}$ is the moment of inertia of the OCT generator (OCTG), $\omega_{\mathcal{R}}$ is the angular rotational speed of the rotor, $T_{\mathcal{R}}$ is the hydrodynamic torque induced on the turbine's rotor, and $T_{\mathcal{E}}$ is the electromagnetic torque generated by the rotor. However, for a steady and homogeneous flow field the rotor speed is typically constant such that $\frac{d\omega_{\mathcal{R}}}{dt} = 0$ and Eq. (1) reduces to $T_{\mathcal{R}} = T_{\mathcal{E}}$.

When turbulence is introduced into the system, the hydrodynamic torque, T_{τ}, on the turbine's rotor can be expressed similarly to Zhang et al. (2017) as:

$$T_{\tau} = T_{\mathcal{R}} + T_{D} \tag{2}$$

where T_D is the deviation of torque resulting from turbulence. Additionally, the rotational speed of the rotor under the influence of turbulence can be redefined as:

$$\omega_{\tau} = \omega_{\mathcal{R}} + \omega_{D} \tag{3}$$

for which ω_D is the rotational speed deviation resulting from turbulent conditions.

With the hydrodynamic torque now analyzed for both constant flow speed and turbulent conditions, the impacts that rotor blade imbalance faults have on hydrodynamic torque can also be analyzed. Additionally, the resulting effects from both imbalance faults and turbulent conditions on the electrical signals output by the OCTG can also be investigated.

To begin, the hydrodynamic torque of an OCT under the influence of turbulence and rotor blade imbalance fault conditions can be re-formulated as, $T_{\mathcal{F}}$, for which:

$$T_{\mathcal{F}} = T_{\mathcal{I}} + T_{\tau} \tag{4}$$

where $T_{\mathcal{I}}$ is the variable torque induced on the rotor shaft stemming from the imbalance fault conditions. Also, the angular rotating speed of rotor can be described as:

$$\omega_{\mathcal{F}} = \omega_{\mathcal{I}} + \omega_{\tau} \tag{5}$$

where $\omega_{\mathcal{I}}$ is the rotational speed deviation caused by the imbalance fault.

To facilitate the investigation of the impacts that rotor blade imbalance faults have on the electrical signals output by the OCTG, the definition of $T_{\mathcal{F}}$ can be reformulated similarly to Gong and Qiao (2013) as:

$$T_{\mathcal{F}} = T_{\tau}(t) + A_{\mathcal{V}} \cdot cos\left(\int 2\pi \cdot f_{\mathcal{F}}\, dt\right) \tag{6}$$

where t is the time index and A_v is the magnitude of the shaft torque variation resulting from the pitch imbalance fault, such that $f_F = \frac{\omega_F}{2\pi}$ is the variable frequency of $T_{\mathcal{F}}$. Furthermore, $T_{\mathcal{F}}$ induces amplitude and frequency modulations (AM and FM respectively) on the generator stator current signal, $I_s(t)$, and its fundamental frequency, $f_s(t)$, such that:

$$I_s(t) = I_{\mathcal{F}}(t) + A_i(t) \cdot sin\left(\int 2\pi \cdot f_{\mathcal{F}}\, dt + \varphi_i\right) \tag{7}$$

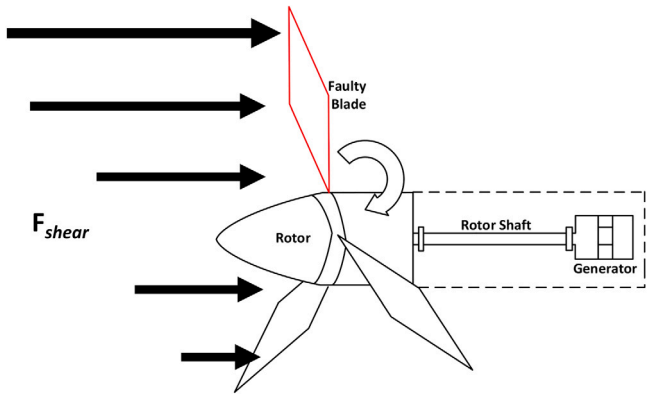

Fig. 1. Figure detailing the effects of current shear, F_{Shear}, on OCT rotor blades. The longer F_{Shear} arrows indicate a larger shear force magnitude.

$$f_s(t) = f_F(t) + A_f(t) \cdot sin\left(\int 2\pi \cdot f_F\, dt + \varphi_f\right) \tag{8}$$

In (7), I_F is the component of the stator current signal stemming from the variability within the ocean current flow velocity resulting from turbulence and the presence of the pitch imbalance fault. Additionally, A_i and ψ_i are the respective amplitude and phase components of the stator current signal that are generated by the pitch imbalance fault. In (8), A_f and φ_f are the respective amplitude and phase components of the stator current's fundamental frequency signal, f_F, stemming from the pitch imbalance fault conditions.

Eqs. (7) and (8) can be combined to formulate a more condensed form of the modulated electrical stator current signal:

$$I_{\mathcal{M}} = I_s(t) \cdot sin\left(\int 2\pi \cdot f_s\, dt\right) \tag{9}$$

for which $I_{\mathcal{M}}$ is the modulated generator stator current signal under the influence of both turbulence and pitch imbalance fault conditions.

Lastly, if it is assumed that an ideal three-phase supply voltage is output from the OCTG, then the three-phase instantaneous power, P, can be expressed as:

$$P(t) = V(t) \cdot I_{\mathcal{M}}(t) \tag{10}$$

where $V(t)$ is the terminal voltage of the stator. The single-phase power output by the generator can therefore be defined similarly to Watson et al. (2010) as:

$$P_s(t) = \frac{\sqrt{3}}{2} \cdot \left\{ \begin{array}{c} V_{LL} I_{sup}[cos(2\omega_s t - \varphi_s) + cos\varphi_s] \\ + \sum_{m=1}^{\infty} \left\{ \begin{array}{l} V_{LL} I_{fault} \left[\begin{array}{c} cos((2\omega_s - m\omega_R)t - \varphi_F) \\ + cos(m\omega_R t + \varphi_F) \end{array} \right] \\ + V_{LL} I_{FF} \left[\begin{array}{c} cos((2\omega_s + m\omega_R)t - \varphi_{FN}) \\ + cos(m\omega_R t - \varphi_{FN}) \end{array} \right] \end{array} \right\} \end{array} \right\} \tag{11}$$

where V_{LL} is the maximum supply line-to-line voltage and φ_s is the initial phase angle of the fundamental supply current. Additionally, I_{sup} is the maximum fundamental supply current, m is a constant positive integer, ω_s is the supply current signal's angular frequency, and I_{fault} is the peak value of the stator current signal's characteristic fault component when the frequency equals $f_s + mf_R$, for which where f_s is the characteristic frequency of I_{sup} and f_R is the rotor shaft's rotational frequency. Finally, φ_F is the initial value of the phase angle when the characteristic fault component has a frequency of $f_s + mf_R$, I_{FF} is the maximum value of the characteristic fault component in the stator current signal at the frequency $f_s - mf_R$, and φ_{FN} is the initial value of the phase angle when the characteristic fault component has a frequency of $f_s - mf_R$.

From this analysis, the following key points can be summarized:

1. As shown in Fig. 1, in the presence of current shear, F_{Shear}, the magnitude of the force induced on the rotor blades at the top of the rotating plane will be greater than the force induced on the blades closer to the bottom of the rotating plane. This results in dynamic loads and vibrations being induced on the turbine's rotor shaft. Due to the electromagnetic coupling that exists between the rotor shaft and generator, the kinetic energy inherent to these dynamic loads and vibrations modulates the OCTG's electrical signals output. These modulations manifest themselves as visible frequency excitations within the frequency spectra of the turbine's electrical signals at the 3P frequency (3 times the shaft rotating frequency).
2. However, when one of the blades is faulty, the forces exerted on the faulty blade near the top of the rotating plane will be different than the forces exerted on the other two blades when they reach the top of the rotating plane. In this scenario, dynamic loads and vibrations will also be induced on the turbine's rotor shaft, however this time at the 1P frequency (shaft rotating frequency) as opposed to the 3P frequency (see Fig. 9).
3. In the presence of turbulence, temporally and spatially varying flow fields leads to differences in magnitudes of F_{Shear} at the top and bottom of the rotor's rotating plane. This reduces the magnitude of dynamic loads and vibrations that are induced on the rotor shaft. This then leads to less pronounced frequency excitations being present in the frequency spectra of the electrical signals output by the OCTG. Additionally, the shaft rotation speed will also vary because of the associated variable current flow velocity that is inherent to turbulence (see Fig. 2). This causes frequency smearing in the frequency spectra of $P_s(t)$, as the characteristic 1P frequency of the rotor shaft will now vary and overlap with the fundamental frequency of the stator current signal, which in itself is also varying.

Therefore, the presence of F_{Shear} increases the ease in detecting imbalance faults, however, the presence of turbulence masks or increases the difficulty in detecting imbalance faults.

3. Proposed fault detection and classification framework

Fig. 3 is a portrayal of our proposed fault detection and severity classification framework. A high level overview of this figure is presented here:

1. Step 1 of the framework begins with the application of a Continuous Wavelet Transform (CWT) on the $P_s(t)$ signals output from the OCTG. Statistical features corresponding to the mean, standard deviation, skewness, kurtosis, peak to peak, and RMS values are extracted from the wavelet coefficients residing within the 1P frequency range of the time–frequency spectrograms created by the CWT.
2. These features are then tabulated into a six-degree feature space, where Principle Component Analysis (PCA) is employed to reduce the dimensionality of the feature space. This lower dimensional feature space is then fed into a multinomial logistic regression machine learning classifier for current flow speed classification.
3. With the current flow speed of $P_s(t)$ now know, turbulence intensity (T.I.) classification can be performed in step 3 of the framework. In this step, the $P_s(t)$ signals output from the OCTG are first categorized according to their newly predicted current flow speeds. Then, once categorized, a new set of time-domain features corresponding to the margin factor, impulse factor, shape factor, crest factor, skew factor, and kurtosis factor are extracted from the signals. These particular time domain features were chosen because they were empirically found to adeptly quantify high frequency fluctuations inherent to $P_s(t)$ signals simulated

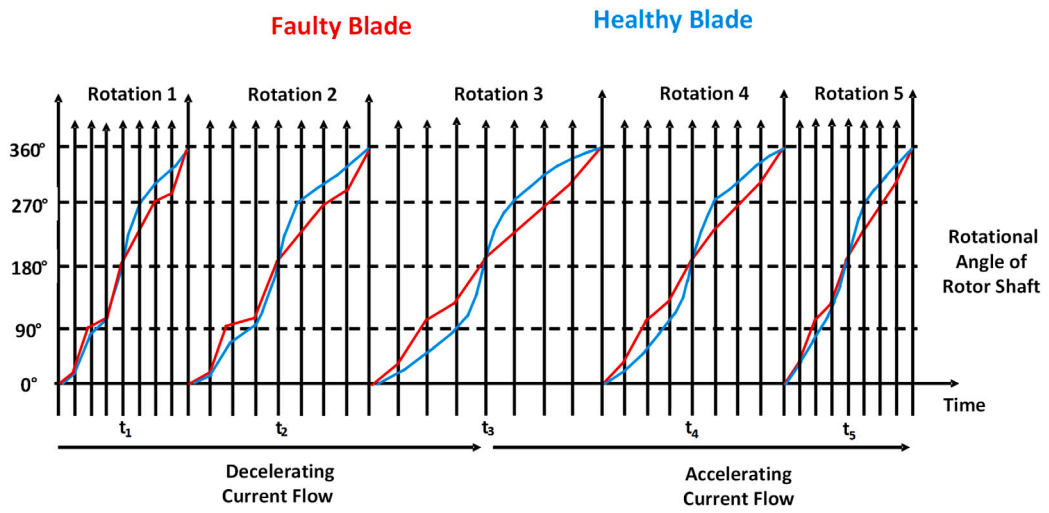

Fig. 2. The presence of turbulence creates a temporally and spatially varying water velocity field, which creates variability in the rotor torque and speed. As depicted in the figure, as the current velocity magnitude increases and decreases, the amount of time needed for the rotor to make a full rotation decreases and increases respectively. Additionally, the smoothness of healthy and faulty sign waves become distorted. Such a phenomenon creates a variable 1P characteristic frequency, which leads to smearing effects in the frequency spectrum of the electrical signals output from the OCT generator. This smearing effects masks the presence of imbalance faults.
Source: Fig. 2 was adapted from Zhang et al. (2017).

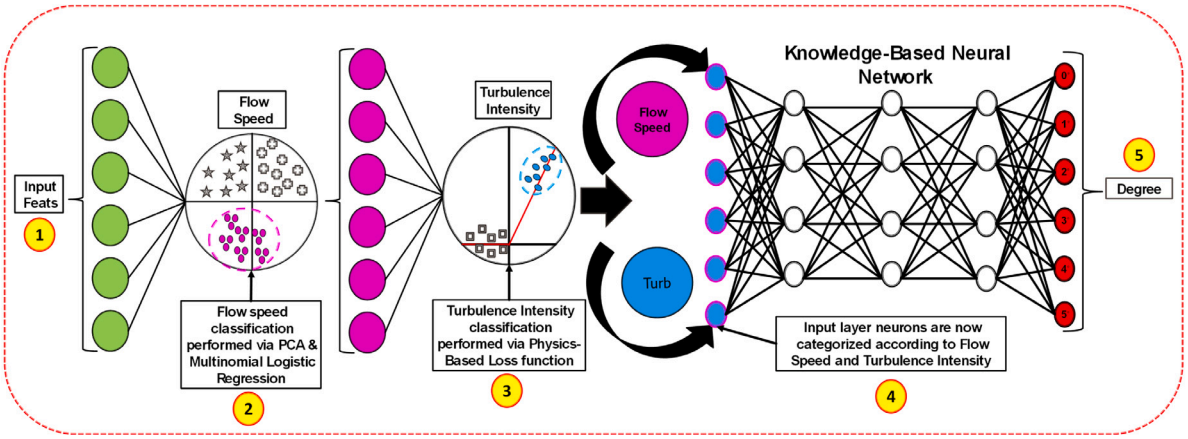

Fig. 3. Schematic diagram of the proposed fault detection and classification framework.

with increasing magnitudes of T.I. Finally, these newly acquired time-domain features are utilized by a physics-guided neural network that constrains model predictions to ensure consistency with the underlying dynamics of the turbine's rotor.

4. With the completion of step 3, both the current flow speed and T.I. labels be assigned to each $P_s(t)$ signal. These labels are combined with the wavelet coefficient statistical feature space that was created in step 1 of the framework. This feature space now consists of the following 8 features: the mean, standard deviation, skewness, kurtosis, peak to peak, RMS, current flow speed and T.I. classification labels. This eight-degree feature space is then fed into a contemporary feed forward neural network.
5. After the neural network in step 4 has been trained, the degree measure of the rotor blade pitch imbalance fault can now be classified via step 5 of the framework.

Each step of the framework will be discussed in greater detail in the following sections. Additionally, a brief background literature synopsis will also be presented for interested readers.

3.1. Time–frequency analysis of generator power signals and input feature acquisition

Fig. 4 provides a more in-depth portrayal of step 1 of our framework. In the left most portion of the diagram, data is simulated by our high-fidelity OCT numerical simulation platform. In the middle portion of the diagram, a CWT is utilized to generate time–frequency spectrograms for each simulated $P_s(t)$ signal. The CWT convolves the generator power signals, $P_s(t)$, with localized wave-like functions of oscillatory nature. These wave-like functions are known as wavelets, and are dilated and translated versions of a single mother wavelet basis function, $\Psi(t)$ (Yan et al., 2014; Addison, 2017). A range of values governing the dilation parameter, **a**, and the translation parameter, **b**, of $\Psi(t)$ can be utilized to increase the CWT's ability to analyze non-stationary signals. When creating spectrogram images, $\Psi(t)$ usually takes on the form, $\Psi(t) = \Psi((t-b)/a)$, for which in the equation below:

$$\mathbf{T}(a,b) = w(a)\int_{-\infty}^{\infty} x(t)\cdot\Psi^*\left(\frac{t-b}{a}\right)dt \tag{12}$$

the quantity $\mathbf{T}(a,b)$ represents the wavelet coefficients, which are measures of cross-correlation between $P_s(t)$ and $\Psi(t)$ (Addison, 2017).

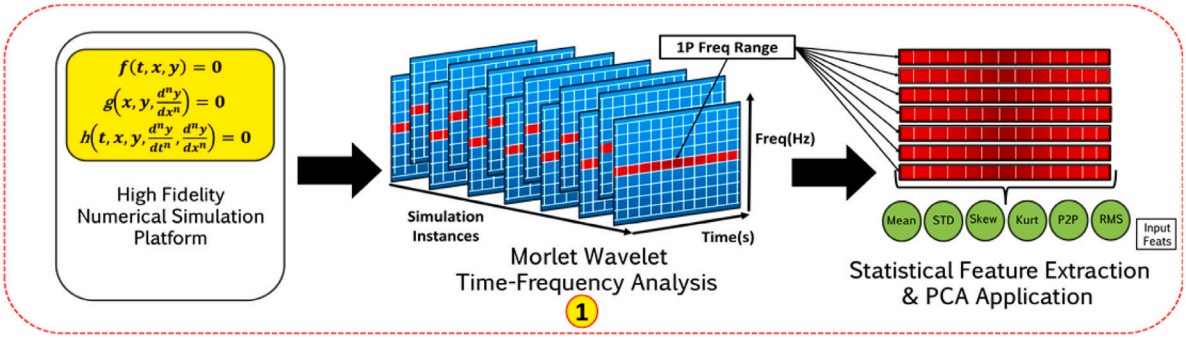

Fig. 4. Flow chart detailing step 1 of the frame work, for which statistical features are extracted from the 1P frequency range of the CWT spectrograms.

Additionally, $w(a)$ is a weighting term that is used to ensure that wavelets of the same scale all possess the same amount of energy, while the * symbol indicates complex conjugation of $\Psi(t)$. When performing the CWT, the optimal $\Psi(t)$ function largely depends on its similarity with the signal being analyzed. For the purposes of this research, the Morlet wavelet was selected as the $\Psi(t)$ of choice because of the similarity of shape between its windowing kernel and the 1P characteristic fault signature within $P_s(t)$. As detailed in Addison (2017), the Morlet wavelet is constructed by tapering a Gaussian window function with a sine wave, such that: $\Psi(t)= e^{2i\pi ft}e^{\left(-t^2/2\sigma^2\right)}$, for which i is the imaginary operator, f is the peak frequency in Hertz of the sine wave, and t is the time in seconds (Cohen, 2019). In this equation, $\sigma = n/2\pi f$, controls the width of Gaussian window, for which n is empirically determined. The term n heavily influences resolution quality, as it controls the Heisenberg uncertainty principle in regards to time–frequency analysis. For our work n was set to range between 5–15.

Lastly, in the right most portion of Fig. 4, the wavelet coefficients encompassed within the 1P band specific frequency range of the spectrograms are concatenated. Then, for each row of this matrix, statistical features corresponding to the Mean, Standard Deviation, Skewness, Kurtosis, P2P, and RMS values are tabulated into a six-degree feature space.

3.2. Dimension reduction of feature space and ocean current flow speed classification

Once the wavelet coefficient statistical feature matrix is constructed, PCA is employed to reduce the dimensionality of the feature space. While there is more than one way to perform PCA, the method used in this research begins with the construction of a covariance matrix, **C-Mat** (Cohen, 2014):

$$\textbf{C-Mat} = (n-1)^{-1}\left(X-\bar{X}\right)\left(X-\bar{X}\right)^T \tag{13}$$

where the n by m data set of wavelet coefficient statistical features is represented by X, with $\bar{X}$ being the mean value of X. Using Matlab's *eig* function, an eigendecomposition is performed on the covariance matrix, such that: $[\mathbf{W},\lambda]= eig\,(\mathbf{X})$. Here, $\mathbf{W}$ is an m by m matrix of the resulting principal components, and λ is a diagonal matrix consisting of the magnitudes of the eigenvalues associated with each principle component.

For the purposes of our research, only the first three principle components are input into a multinomial logistic regression machine learning algorithm for current flow speed classification. Multinomial logistic regression is a machine learning algorithm that assumes that a linear relationship exists between the log odds of the dependent and independent variables of a multi-class data set (Moon and Kim, 2020). When performing multinomial logistic regression with J classes, one class is usually designated as the "piviot", for which J-1 binary independent logistic regression models are constructed. In the case when the Jth class is designated as the "piviot", the regression model for class J becomes (Moon and Kim, 2020):

$$ln\frac{PR(Y=j)}{PR(Y=J)} = \mathbf{b}_j \cdot \mathbf{x} \tag{14}$$

In the above equation, the value of Y represents the outcome of the random variable, where $\mathbf{b}_j$ is the set of regression coefficients for class j and are usually estimated according to the maximum likelihood method, while $\mathbf{x}$ is the vector of observed features. Thus, the probability that any instance of $\mathbf{x}$ belongs to class j can be expressed as:

$$PR(Y=j) = PR(Y=J)\cdot e^{\mathbf{b}_j\cdot\mathbf{x}} \tag{15}$$

Lastly, because the probability that $\mathbf{x}$ belonging to each class must equal 1, the probability that $\mathbf{x}$ belongs to class $\mathbf{J}$ is:

$$PR(Y=j) = \frac{e^{\mathbf{b}_j\cdot\mathbf{x}}}{1+\sum_{j=1}^{J-1} e^{\mathbf{b}_j\cdot\mathbf{x}}} \tag{16}$$

Therefore, as derived in Moon and Kim (2020), when given the truncated eigenvector feature matrix, $\mathbf{x}$, the probability that any instance will have a class label of $\mathbf{y}$ is:

$$y = argmax_j\ PR(Y=j) \tag{17}$$

3.3. Turbulence intensity prior knowledge infusion

Once each individual $P_s(t)$ signal has had its current flow speeds classified, a new set of time-domain features are extracted from the signals to create a new feature space. The set of time-domain features extracted from these signals are the margin factor, impulse factor, shape factor, crest factor, kurtosis factor, and skewness factor. These features have demonstrated a high proficiency at quantifying the magnitude of the impulsiveness within the $P_s(t)$ signals (Ali et al., 2018; Li et al., 2020a). Since turbulence intensity was empirically found to most prevalently expresses itself as a high frequency fluctuations within $P_s(t)$, these features are used to construct this entirely new feature space.

As depicted in Fig. 5, our framework integrates both the physics-based prior knowledge obtained from the oceanic environment (VanZwieten et al., 2013), and the new T.I. time-domain features into the machine learning pipeline of a neural network. The T.I.-based prior knowledge incorporation is made via the inclusion of a physics-based loss function, which ensures that model predictions remain scientifically consistent with the underlining physics of the OCT's rotor. When these T.I. time-domain features are merged with the environmental-based prior knowledge, the neural network is allowed to learn from both inputs in a symbiotic-like fashion.

The T.I. classification portion of our framework begins by considering the time-domain features describing the nature of $P_s(t)$ when the rotor is under the influence of turbulence, a variable current flow, and imbalance fault conditions. Initially, this feature set, $\mathbf{U}$, consists of the T.I.-based time-domain features, $\mathbf{F}_T$, and their correlated current flow speed labels, $\mathbf{F}_S$, which were predicted in step 2 of the framework:

$$\mathbf{U} = \left[\mathbf{F}_T, \mathbf{F}_S\right] \tag{18}$$

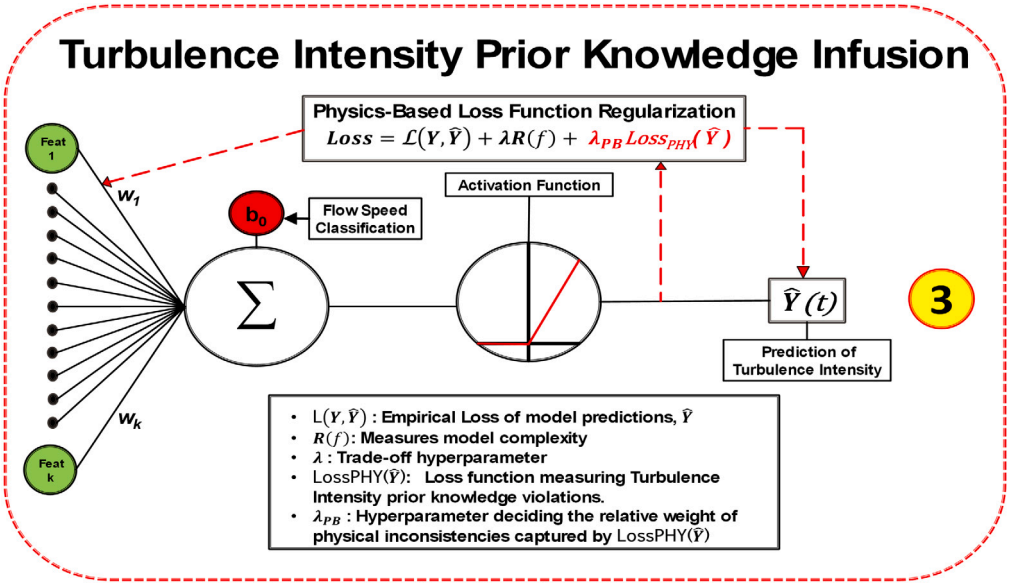

Fig. 5. Schematic detailing how a key physical relationship existing between T.I. and $P_s(t)$ are leveraged to construct a physics-based loss function. Time-domain features characterizing $P_s(t)$ are fed into a feed-forward neural network. During training, a physics-based loss term is appended to the loss function of the neural network to penalize T.I. classifications that violate the physical relationship existing between T.I. values and $P_s(t)$.

In a similar fashion to the work done in Karpatne et al. (2017), our framework can adopt a basic multi-layer perceptron architecture to classify T.I. for any instance of **U**. In the case of a fully connected neural network, with L hidden layers, the following modeling equations, also derived from Karpatne et al. (2017), can be used to correlate instances of $\mathbf{u}$ to their target prediction $\hat{\mathbf{y}}$ as:

$$\mathbf{z}_1 = \mathbf{W}_1^T \cdot \mathbf{u} + \mathbf{b}_1 \tag{19}$$

$$\mathbf{z}_i = \mathbf{W}_i^T \cdot \mathbf{a}_{i-1} + \mathbf{b}_i, \ \forall_i = 2 \text{ to } L \tag{20}$$

$$\mathbf{a}_i = f\left(\mathbf{z}_i\right) \ \forall_i = 1 \text{ to } L \tag{21}$$

$$\hat{\mathbf{y}} = \mathbf{W}_{L+1}^T \cdot \mathbf{a}_L + \mathbf{b}_{L+1} \tag{22}$$

where in the above equations, $(\mathbf{W}, \mathbf{b})$ represents the set of all weight and bias terms present throughout all hidden and output layers, with $f(\cdot)$ acting as the hidden layer activation function.

3.4. Construction of the physics-based loss function

Customarily, when training a neural network, the goal is to minimize the empirical loss of $\hat{\mathbf{Y}}$ while also maintaining the lowest possible model complexity. This can be achieved as demonstrated in the formula below:

$$\text{argmin}_f = \text{CE}_{Loss}\left(\hat{\mathbf{Y}}, \mathbf{Y}\right) + \lambda \mathbf{R}(\mathbf{W}) \tag{23}$$

for which a multi-class cross-entropy loss function, CE_{Loss}, is used. Here, CE_{Loss}, is defined as Moon and Kim (2020):

$$\text{CE}_{Loss} = -\sum_{c=1}^{M} y_{o,c} \log\left(p_{o,c}\right) \tag{24}$$

where M represents the number of class labels, y is the binary indicator attesting if the class label, c, is correct for a given observation, o, and for which p is the predicted probability that observation, o is indeed of class, c. Additionally, from (23), **R**, is a function that measures model complexity, in which λ_1 and λ_2 are trade off hyper-parameters, such that according to Karpatne et al. (2017):

$$\lambda \mathbf{R}(\mathbf{W}) = \lambda_1 \|\mathbf{W}\|_1 + \lambda_2 \|\mathbf{W}\|_2 \tag{25}$$

To alleviate some of the inconsistencies that exists between $\hat{\mathbf{Y}}$ and $\mathbf{Y}$, a physics-based loss term, as proposed in Karpatne et al. (2017) is incorporated into the model's empirical loss function:

$$\mathbf{Loss} = \mathcal{L}\left(\mathbf{Y}, \hat{\mathbf{Y}}\right) + \lambda R(f) + \lambda_{PB} \mathbf{Loss}_{PHY}\left(\hat{\mathbf{Y}}\right) \tag{26}$$

Here, $\mathcal{L}\left(\mathbf{Y}, \hat{\mathbf{Y}}\right)$ is the empirical error of the model predictions, where again, the function $R(f)$ measures the complexity of the model, with λ being a trade off hyper-parameter. However, in this particular version of the loss function, the term $\mathbf{Loss}_{PHY}\left(\hat{\mathbf{Y}}\right)$ is added to penalize physics-based violations of the model predictions and λ_{PB} is a physics-based hyper-parameter that decides upon the importance of the inconsistencies captured by $\mathbf{Loss}_{PHY}\left(\hat{\mathbf{Y}}\right)$.

From the investigations performed in our research, which analyzed the affects of certain oceanic environmental parameters on $P_s(t)$, our framework was able to discover and leverage a key physical relationship that exist between T.I. and $P_s(t)$. Our framework used this relationship as a form of prior knowledge to aid in the development of our physics based loss function. This key physical relationship can be explained by first formally defining T.I according to TSI (2012):

$$\mathbf{TI} = \frac{\sqrt{\sigma_x^2 + \sigma_y^2 + \sigma_z^2}}{\bar{V}} \tag{27}$$

where σ_x, σ_y, and σ_z represent the standard deviation of the current flow velocities in the x,y, and z directions, while $\bar{V}$ represents the mean current velocity. Then, as stated in Pyakurel et al. (2017), we take note that the standard deviation of $P_s(t)$ increases with increasing T.I. Combining this bit of information with the fact that, within the turbulence energy spectrum, small scale turbulence and its associated higher frequency components obey a -5/3 slope (Chasnov, 1991), we were able to derive a relatively accurate way of approximating a metric that is proportional to T.I., abbreviated below as $\mathbf{TI}_{approx}$:

$$\mathbf{TI}_{approx} = \left[\frac{\mathbf{STD}\left(P_s\right)}{\bar{P}_s}\right]^{\left(-\frac{5}{3}\right)} \tag{28}$$

where $\bar{P}_s$ is the mean value of P_s and $\mathbf{STD}(\cdot)$ is the standard deviation function operator.

For an OCT operating with an average current flow velocity of $\bar{V}$, the relationship that exists between $\mathbf{STD}\left(P_s\right)$ when the T.I. is

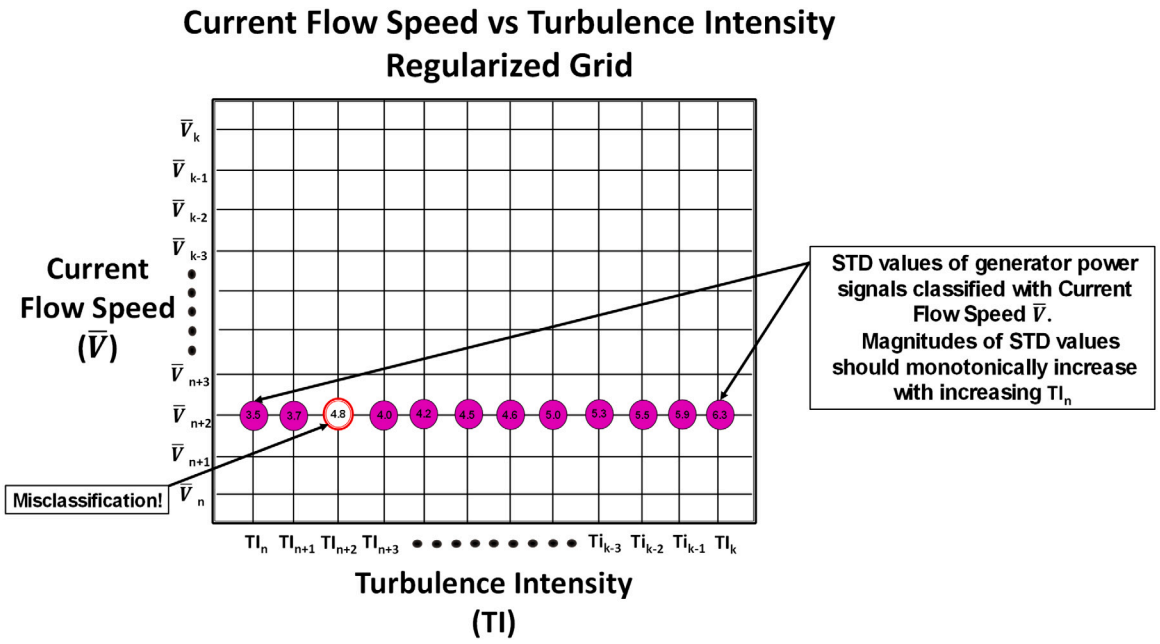

Fig. 6. Display of a regularized grid of T.I. values populated along the x-axis and $\bar{V}$ values populated along the y-axis. For all $P_s(t)$ signals simulated with the same $\bar{V}$, the magnitude of $\mathbf{STD}\left(P_s\right)$ should monotonically increase with increasing T.I.

approximately $\mathbf{TI}_{approx.(n)}$, and $\mathbf{STD}\left(P_s\right)$ when the T.I. is approximately $\mathbf{TI}_{approx.(n+1)}$, can be formally described as:

$$\mathbf{STD}\left(\mathrm{P}_s\right)_{\mathbf{TI}_{approx.(n)},\bar{V}} - \mathbf{STD}\left(\mathrm{P}_s\right)_{\mathbf{TI}_{approx.(n+1)},\bar{V}} \leq 0, \text{if } \mathbf{TI}_{approx.(n)} \leq \mathbf{TI}_{approx.(n+1)} \quad (29)$$

In words, Eq. (29) simply states that for the same $\bar{V}$, the standard deviation of $P_s(t)$ increases with increasing T.I. This concept can be visualized more succinctly in Fig. 6. To leverage this relationship was when classifying T.I., a physics-based loss function was constructed as follows:

1. Consider an unlabeled set of $\mathbf{STD}\left[P_s\right]$ values that are mapped onto a regularized grid of T.I. by $\bar{V}$ values, such as those shown in Fig. 6. In such a scenario, the difference in $\mathbf{STD}\left[P_s\right]$ values simulated with the same $\bar{V}$ value, but with different $\mathbf{TI}_{approx}$ values can be described as:

$$\Delta\mathbf{STD}\left[\mathrm{P}_s\right]_{\mathbf{TI}_{approx},\bar{V}} = \mathbf{STD}\left[\mathrm{P}_s\right]_{\mathbf{TI}_{approx.(n)},\bar{V}} - \mathbf{STD}\left[\mathrm{P}_s\right]_{\mathbf{TI}_{approx.(n+1)},\bar{V}} \quad (30)$$

where a positive value of $\Delta\mathbf{STD}\left[\mathrm{P}_s\right]_{\mathbf{TI}_{approx},\bar{V}}$ would be interpreted as a violation of the key physical relationship described in (29).

2. Therefore, in a similar fashion as to what was derived in Karpatne et al. (2017), our physics-based loss term can be defined as:

$$\mathbf{Loss}_{PHY}\left(\hat{\mathbf{Y}}\right) = \frac{1}{\bar{\mathbf{V}}_{\mathbf{n}} \cdot \left(\mathbf{TI}_{approx.(n-1)}\right)} \cdot \sum_{\bar{V}_n}^{\bar{V}_n} \cdot \sum_{\mathbf{TI}_n}^{\mathbf{TI}_{n-1}} \cdot \mathbf{RELU}\left(\Delta\mathbf{STD}\left[\mathrm{P}_s\right]_{\mathbf{TI}_{approx},\bar{V}}\right) \quad (31)$$

where the mean value of all $\Delta\mathbf{STD}\left[\mathrm{P}_s\right]_{\mathbf{TI}_{approx},\bar{V}}$ violations across every T.I. x $\bar{V}$ coordinate can be evaluated by the ReLU activation function.

3. Lastly, the physics-based loss term is re-implemented back into the original empirical loss function, such that:

$$\mathbf{Loss} = \mathcal{L}\left(\mathbf{Y}, \hat{\mathbf{Y}}\right) + \lambda R(f) + \frac{\lambda_{PB}}{\bar{\mathbf{V}}_{\mathbf{m}} \cdot \left(\mathbf{TI}_{approx.(n-1)}\right)} \cdot \sum_{\bar{V}_m}^{\bar{V}_m} \cdot \sum_{\mathbf{TI}_n}^{\mathbf{TI}_{n-1}} \cdot \mathbf{RELU}\left(\Delta\mathbf{STD}\left[\mathrm{P}_s\right]_{\mathbf{TI}_{approx},\bar{V}}\right) \quad (32)$$

Fig. 5 can be referenced for more details on how this loss function integrates back into our overall framework.

4. Numerical simulation validation and data set preparation

4.1. Validation of our high fidelity numerical simulation platform

While the work performed in this research does not use data generated by an in service OCT, geometric and inertial properties derived from the experimental OCT pictured in Fig. 7 were used to create the utilized high fidelity numerical simulation platform. This 20-kW experimental OCT was fabricated and deployed into the South Florida Gulf Stream by Florida Atlantic University's Southeast National Marine Renewable Energy Center (SNMREC). Additionally, spatiotemporal environmental data, acquired from an ADCP, were used to further increase model fidelity (VanZwieten et al., 2013; Tian et al., 2016).

The research performed in VanZwieten et al. (2013) and Tian et al. (2016) investigated ways in which marine environmental conditions impacted OCT performance. Insights from these studies were used to validate and fine-tune modeling algorithms within the SNMREC numerical simulation platform. The CFD based analyses performed in these studies quantified, among other things, the effects of ambient current flow velocity and turbulence intensity on the performance of the SNMREC prototype OCT. Additionally, the following flow statistics obtained from the 13-month measurement campaign described in VanZwieten et al. (2013) and Tian et al. (2016) were utilized:

- The mean ocean current speed at a depth of 20 m is 1.6 m/s, with the overall current speed at this depth ranging between 0.4 and 2.5 m/s.
- The average measured vertical current shear was 0.004 [m/s]/m.

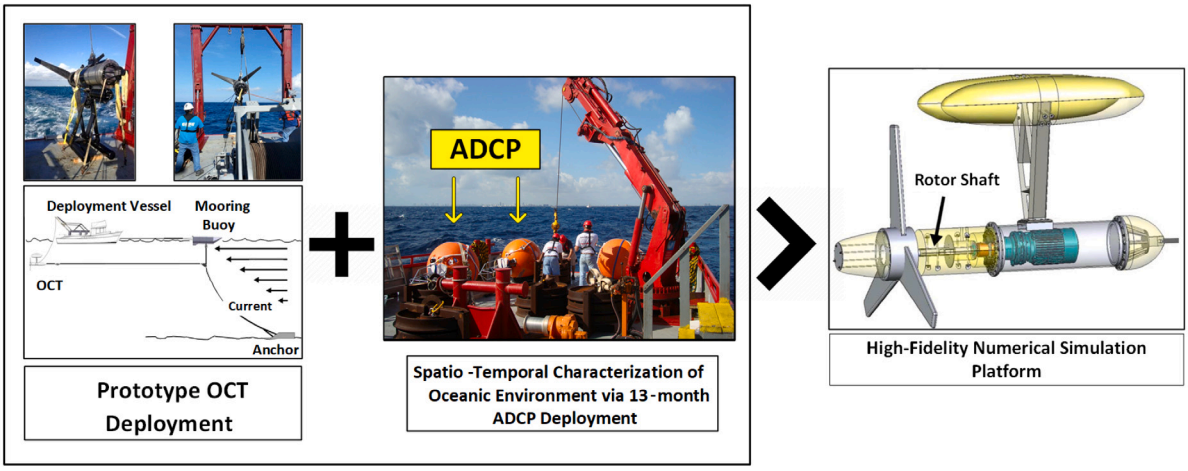

Fig. 7. A high level overview of the numerical simulation platform used to generate data for this study. Operational performance data as well as a variety of other geometric and inertial properties are obtained from the SNMREC 20-kW prototype OCT. This data is primarily used as a modeling aid for the simulation platform. Additionally, spatiotemporal oceanic environmental data, as profiled by an ADCP, is used to further increase the modeling fidelity of the simulation platform.

Table 1
Overview of simulation platform data generation.

Length: 120 s Sampling Frequency: 200 Hz Num. of Sims: Source=500/Target=50			
Parameters	Parameter range	Step size increment	Simulations per step
Turbulence intensity	10%	5%	50
Current flow speed	0.4 m/s–2.4 m/s	0.4 m/s	50
Pitch imbalance	0 Deg–5 Deg	1 Deg	50

These measurements were utilized to set the operating parameters of the numerical simulation platform during data generation. Our numerical simulation platform was developed using a Blade Element Momentum (BEM) rotor modeling technique that uses a dynamic wake inflow model (VanZwieten et al., 2013). This BEM algorithm is similar to the AeroDyn aerodynamics code utilized within NREL's FAST wind turbine simulator. NREL's FAST wind turbine simulator has been certified by Germanischer Lloyd for turbine design and analysis.

NREL's WTPerf code was used to validate our simulation platform's hydrodynamics model. This validation found peak power and thrust coefficients of 0.447 and 0.694 using our numerical simulation platform, while values of 0.444 and 0.685 were respectively calculated using NREL's WTPerf code (VanZwieten et al., 2013). NREL's HarpOpt code was used to create our variable pitch rotor model design to help ensure appropriate rotor geometry values such as cord lengths twist angles were utilized (VanZwieten et al., 2016). The turbulent flow field was mathematically constructed using algorithms discussed in Pyakurel et al. (2017), which includes a method for modeling spatial flow coherence over the swept area of the rotor. Lastly, the degrees of freedom of the OCT were limited to the rotation of the rotor about its axis, which is the "Tidal Turbine" version of the numerical simulation platform presented in Tzelepis et al. (2017).

4.2. Simulation setup and data set preparation

Table 1 provides an overview of the environmental parameters used to simulate OCT performance data for this work. The ranges for these values were obtained from the 13-month ADCP study summarized in VanZwieten et al. (2013) and Tian et al. (2016), with the turbulence intensity range derived from measurements recorded at potential tidal energy sites. In total, 50 random seeds were utilized when running simulations for each turbulence intensity, flow speed, and pitch imbalance combination depicted in Table 1. Thus, 7200 individual simulations were run. For each case, the turbulence intensity, current flow speed, and degree of the pitch imbalance fault parameters were varied. The time length of each simulation was 115 s, and the sampling frequency was 200 Hz. However, to account for the turbine's ramp-up time, only the last 50 s of data were used from each simulation. Lastly, the average rotor speed was maintained near the targeted operating speed associated with maximum power production through the use of a fixed gain torque controller, $\tau = k \cdot \omega^2$. However, it should be noted that "average speed" does not imply "constant speed", as investigating variable speed rotor dynamics is more representative of real world operating conditions, and thus more beneficial to both the academic and commercial OCT communities overall.

Fig. 8 displays the $P_s(t)$ signals simulated for the zero-degree (healthy) fault case for seed one of the data set. Plots (a)–(f) hold a specific current flow speed value constant while the T.I. is allowed to vary discreetly according to the values specified in parameter range column of Table 1. As shown, even in the healthy state, the morphology of $P_s(t)$ varies greatly with respect to the external operating environment. A salient trend, correlating high frequency fluctuation with increasing magnitudes of current flow speed and T.I. can be seen to exist. Thus, the primary objective of our framework is to establish a consistent means of accurately quantifying the differences between healthy and fault rotor blade states regardless of the external environmental parameters that any particular $P_s(t)$ signal may have been simulated with.

5. Quantification of simulation results

5.1. Justification for taking a physics-guided approach

In order to motivate a discussion concerning the justification of implementing a physics-based learning approach into our framework, first reference Fig. 4, in which statistical input features are extracted from the 1P band specific frequency range of the CWT spectrograms. Fig. 9 portrays an instance of these spectrogram, for which two signals contained within seed 1 of the data set are depicted. In both instances, the characteristic 1P frequency range of interest is highlighted, and an average current flow speed of 0.8 m/s was maintained. However, Fig. 9(a), displays a 5-Degree imbalance fault case simulated with 20%

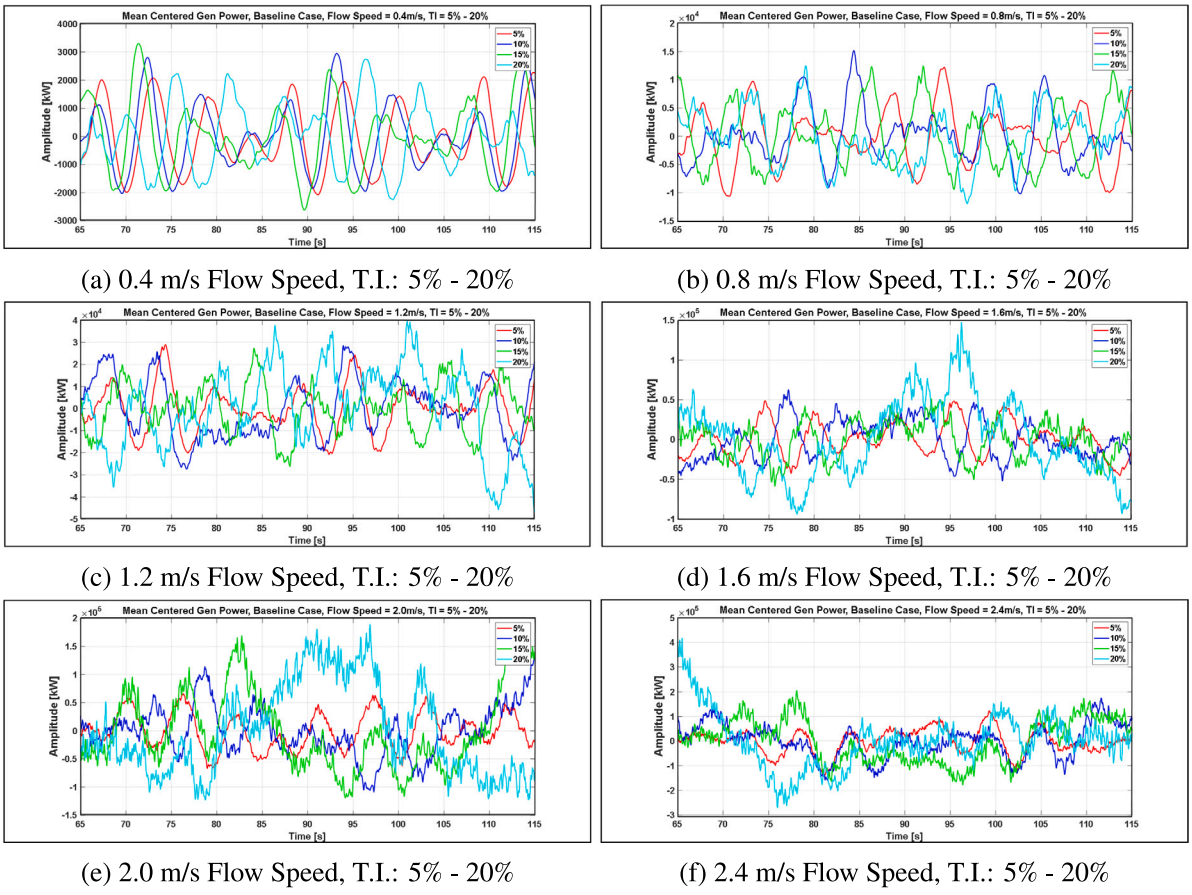

(a) 0.4 m/s Flow Speed, T.I.: 5% - 20%

(b) 0.8 m/s Flow Speed, T.I.: 5% - 20%

(c) 1.2 m/s Flow Speed, T.I.: 5% - 20%

(d) 1.6 m/s Flow Speed, T.I.: 5% - 20%

(e) 2.0 m/s Flow Speed, T.I.: 5% - 20%

(f) 2.4 m/s Flow Speed, T.I.: 5% - 20%

Fig. 8. Representative look at the 0-degree fault case for seed 1 of the data set. In each of the plots (a)–(f) the average current flow speed is held constant while the T.I. is allowed to vary. Take note of the extents to which the signal morphology changes as the magnitude of the current flow speed and T.I. parameter values increase. Despite the dynamic changes in signal morphology, all of the depicted time-series signals are simulated for healthy states of the rotor.

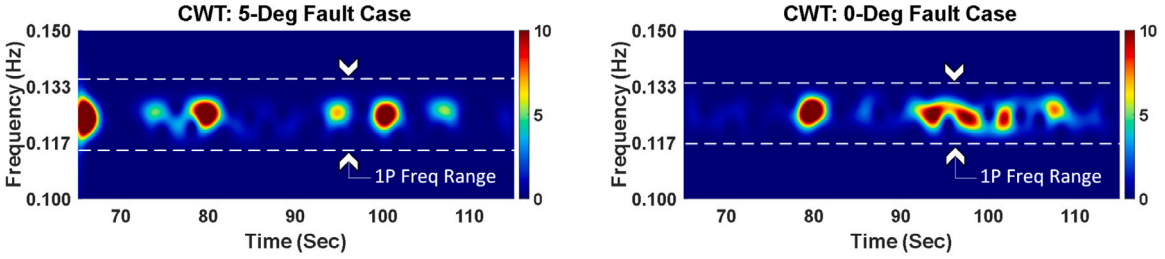

(a) 0.8 m/s Flow Speed, 5-Deg Fault Case, 20% T.I.

(b) 0.8 m/s Flow Speed, 0-Deg Fault Case, 5% T.I.

Fig. 9. The high degree of similarity between the two CWT spectrograms is highlighted. Such similarities depict the challenge of performing fault detection when oceanic operating parameters are allowed to vary according to their natural ranges. (a) displays a 5-Deg fault case, and (b) displays a 0-Deg fault case. In particular, notice how the frequency activity within the 1P frequency range of interest is roughly the same despite the fault severity diapason.

T.I., while in Fig. 9(b) portrays a 0-Degree (healthy) imbalance fault case simulated with 5% T.I.

Now consider Table 2, which lists the names and mathematical formulas of the features used to train the machine learning algorithms utilized within our framework. Of special note is the Adjusted *P*-value column, which quantifies the magnitude of the statistical difference between features extracted from the spectrogram displayed in Fig. 9(a), and the features extracted from the spectrogram corresponding to Fig. 9(b). As shown in the Adjusted *P*-value column of Table 2, all of the features have a P-value > 0.05. This implies that there is no statistically significant difference between features extracted from Fig. 9(a) and those extracted from Fig. 9(b), despite the fact that Fig. 9(a) represents the most severe fault case contained within our study, while Fig. 9(b) represents a completely healthy non-fault case.

The lack of distinction between fault cases is blurred as oceanic environmental parameters are allowed to vary in accordance to their full dynamic ranges. Recall that as highlighted at the end of Section 2, the presence of turbulence masks or increases the difficulty of performing imbalance fault detection. Difficulties such as these help to illustrates the need of including a physics-guided methodology within our framework. Such methodologies are especially adept at discovering salient trends hidden deep within the data and thus lend themselves well to incipient fault detection.

5.2. Current flow speed and turbulence intensity classification

The first step that our framework employs when classifying rotor blade pitch imbalance faults is to determine the current flow speed that

Table 2
Proposed input features with adjusted P-vals. *P-Values acquired from Fig. 3 Investigation, **Flow Speed feature provided by step 2 of framework, ***T.I. feature provided by step 3 of framework.

Proposed fault detection input features w/ Adj. P-vals			
Number	Feature	Mathematical equation	Adj. P-value*
1	Mean	$\mu = \frac{1}{N}\sum_{i=1}^{N} x_i$	0.2975
2	Standard deviation	$\sigma = \sqrt{\frac{1}{N}\sum_{i=1}^{N}\left(x_i - \bar{x}\right)^2}$	0.0527
3	Skewness	$mu_3 = \frac{\sum_{i=1}^{N}(x_i-\bar{x})^3}{(N-1)*\sigma^3}$	0.351
4	Kurtosis	$\mu_4 = \frac{\sum_{i=1}^{N}(x_i-\bar{x})^4}{\sum_{i=1}^{N}(x_i-\bar{x}^2)^2}$	0.0941
5	Peak-to-Peak	$P_2P = max(x) - min(x)$	0.301
6	Root-Mean-Squared	$RMS = \sqrt{\frac{1}{N}\sum_{i=1}^{N}\left(x_i\right)^2}$	0.298
7	Crest factor	$CF = max(x)/RMS$	0.0762
8	Shape factor	$SF = RMS(x)/mean[abs(x)]$	0.0982
9	Impulse factor	$IF = max(x)/mean[abs(x)]$	0.0661
10	Margin factor	$MF = max(x)/mean[abs(x)]^2$	0.08562
11	Skewness factor	$kewFact = \sum_{i=1}^{N}\left(x_i - \bar{x}\right)^3/\left(N*\sigma^3\right)$	0.07215
12	Kurtosis factor	$KurtFact = \sum_{i=1}^{N}\left(x_i - \bar{x}\right)^4/\left(N*\sigma^4\right)$	0.09934
13	Flow speed	N/A	N/A**
14	Turbulence intensity	N/A	N/A***

a particular instance was simulated under. While the current flow speed in itself is not a particularly useful feature when classifying imbalance faults, T.I. is. However, as depicted in Eq. (27), it is necessary to know the current flow speed in order to predict T.I.

Fig. 10(a) depicts the principle component feature space associated with current flow speed prediction. This projection matrix was constructed using features 1–6 of Table 2, and as shown in Fig. 10(b), approximately 97% of the total variance can be captured within the first three principle components alone. This projection matrix was then input into a multinomial logistic regression machine learning classifier, where, from the confusion matrix presented in (c), a classification accuracy of 95.64% is achieved. Next, these predicted current flow speed labels are concatenated with features 7–12 of Table 2 and input into the physics-guided neural network portion of our framework for turbulence intensity classification. Through the use of the neural network's physics-guided loss function, a 98.19% turbulence intensity classification accuracy is obtained. Additional details regarding the construction of this physics-guided neural network are discussed in Section 5.3.

5.3. Imbalance fault degree classification

To demonstrate the effectiveness of our proposed fault detection framework, we compared its performance with the baseline and intermediary methods discussed below. $P_s(t)$ signals were simulated in accordance with the oceanic environmental parameters as shown in Table 1. This ensured that the distributions of their environmental parameters (T.I., current flow speed, and the degree of the pitch imbalance fault) varied with each other in the same manner that they would for an OCT deployed at sea for a sustained length of time. The size of the data set consisted of 7,200 simulations, for which the results from the 10% partitioned test set are shared. Input features 1–12, as shown in Table 2, are collected from each instance and are used in some capacity to train the machine learning models listed below. The neural network models utilized in this work are implemented using the tensor flow 2.0 backend of Keras, for which the Adam optimizer was used to perform stochastic gradient decent. Fully connected neural networks were constructed with 3 hidden layers consisting of 6 nodes each. Lastly, the λ_1 and λ_2 hyper-parameters of (25) were set equal to 1 for all experiments to ensure that no special hyper-parameter tuning was used for any specific experimental scenario.

Repeated 10 fold cross validation was performed, for which random initializations of the neural network weights between 0 and 1 was used during model training to allow for the mean and standard deviation of the evaluated models to be presented in Fig. 11. Listed below are explanations of the different machine learning models that were used to help test the validity and robustness of our proposed fault detection framework.

- **Purely Data-Driven Approach:** Before analyzing the value gained from incorporating current flow speed and T.I. prior knowledge integration into our framework's machine learning pipeline, we wanted to first observe the baseline performance of a purely data-driven approach at addressing the pitch imbalance fault problem. To accomplish this we predicted the severity of several different pitch imbalance faults through the use of a multinominal logistic regression (MLR), a k-nearest neighbor (KNN), and a classic artificial neural network (ANN). Each model was trained using input features 1–12, as described in Table 2, and did not include any physics-based prior knowledge information relating to the current flow speed or turbulence intensity.
- **Knowledge-Based Data-Driven Approach:** To aid in understanding the impact of including current flow speed prior knowledge into the machine learning pipeline of our fault detection framework, we analyzed the performance of the MLR, KNN, and ANN machine learning models with this knowledge included in the input feature set. For this specific scenario, the machine learning models are now designated as: MLR_{KB}, KNN_{KB}, and ANN_{KB}, and include features 1–13 from Table 2. (Feature 13 was predicted in step 2 of our proposed fault detection framework, shown in Fig. 3).
- **Physics-Guided Prior Knowledge Approach:** Lastly, to validate the benefit of the physics-informed loss function developed in Section 3.3, 3.4, and displayed in Fig. 5, a T.I. label, depicted as feature 14 in Table 2, is included in the input feature set of the machine learning models. Due to the incorporation of the physics-informed T.I. label, this subset of machine learning models are designated as: MLR_{Phy}, KNN_{Phy}, and ANN_{Phy}, for which features 1–14, as listed in Table 2, are used to train these models.

Fig. 11 portrays the classification accuracy obtained from the different machine learning models used to validate our fault detection framework. Fig. 11 is comprised of machine learning models that used a purely data driven approach (MLR, KNN, and ANN) to address the imbalance fault problem, the use of knowledge-based machine learning models (MLR_{KB}, KNN_{KB}, and ANN_{KB}) that incorporate the use of current flow speed prior knowledge integration, and physics guided approaches (MLR_{Phy}, KNN_{Phy}, ANN_{Phy}) that incorporate the use of a physics-based loss function for T.I. classification. As depicted in the figure, the purely data driven models demonstrate the lowest accuracy. The low accuracy stems from there being no statistical difference amongst features of differing fault classes that were simulated with different oceanic environmental operating parameters. Specifically, it is very difficult for the data driven models to discern between features simulated with a common current flow speed but a different T.I. and imbalance fault degree measures. As shown in Table 3, the MLR, and KNN models possess a classification accuracy within the 15%-37.5% range, and while the performance of the ANN model was noticeably better, at 39%–56%, this accuracy range was still unsatisfactory.

When compared to the data driven models, the machine learning models that utilized the current flow speed prior knowledge integration (MLR_{KB}, KNN_{KB}, and ANN_{KB}) demonstrated improved accuracy when performing fault detection. Specifically, the MLR_{KB}, KNN_{KB} models are shown to have a classification accuracy that ranges between 45%–60%, while the ANN_{KB} model attains a higher accuracy, ranging between 64%–74%. However, the ceiling of the maximum achievable accuracy score is still capped for these knowledge-based model because knowing the current flow speed that a particular instance was simulated at still does not address the difficulty associated with distinguishing between

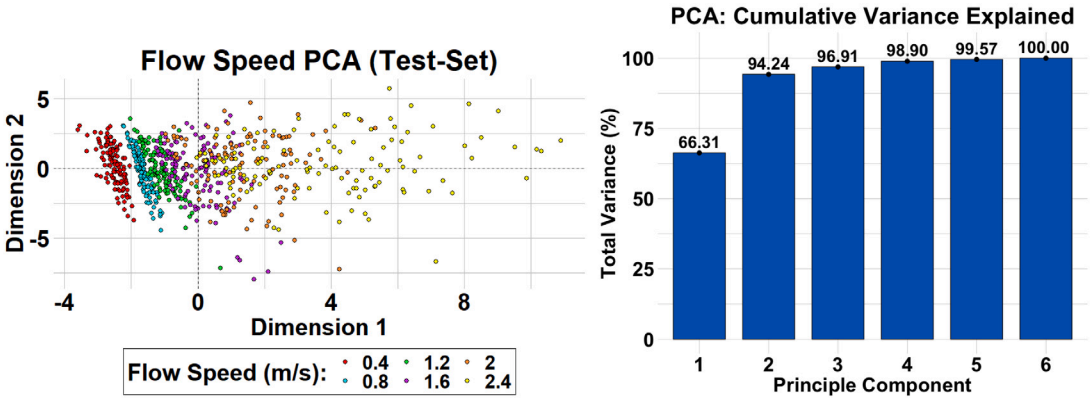

(a) PCA Projection Matrix (b) Cumulative Variance

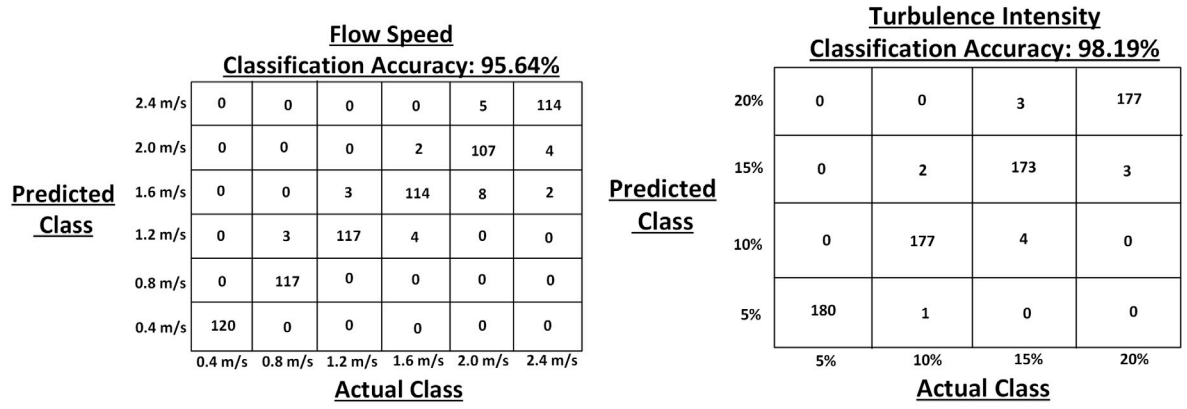

(c) Current Flow Speed Confusion Matrix (d) Turbulence Intensity Confusion Matrix

Fig. 10. Current flow speed and T.I. classification results. (a) 2D projection matrix obtained when PCA is employed on features 1–6 of Table 2. (B) Cumulative variance explained from the principle component analysis. As shown, more than 95% variance is captured from the first three principle components alone. (c) Confusion matrix obtained after multinomial logistic regression is employed to predict the current flow speed. (d) Confusion matrix obtained after the physics-informed loss function is employed to predict turbulence intensity.

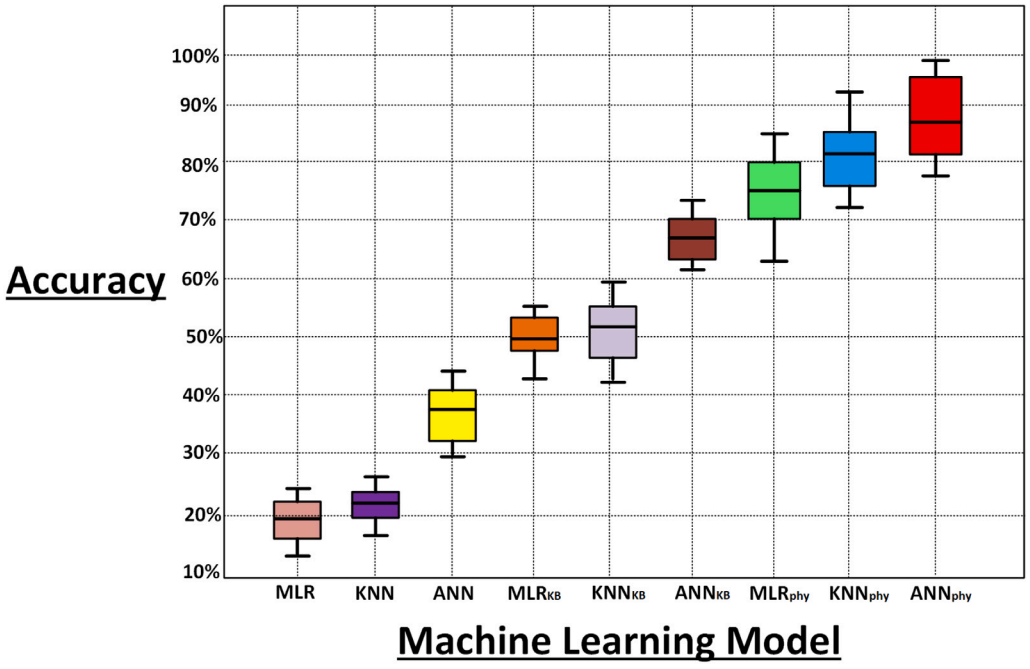

Fig. 11. Box plots portraying the classification accuracy of different machine learning algorithms used to justify the validity of our framework. The figure is comprised of purely data-driven (MLR, KNN, and ANN), prior knowledge integration approaches (MLR_{KB}, KNN_{KB}, and ANN_{KB}), and physics-guided approaches (MLR_{Phy}, KNN_{Phy}, and ANN_{Phy}). The data-driven and knowledge integrated approaches perform less favorably than the approaches physics guided approaches.

features that were simulated with the same current flow speed but different T.I. values.

When considering instances simulated with one particular current flow speed, an overwhelming majority of the miss-classifications were instances possessing high T.I. values and high imbalance fault degree measures. Deeper analysis of this trend found that the statistical nature of the wavelet coefficient energy residing within the 1P frequency range of these instances was quite similar to the statistical nature of the wavelet coefficient energy residing within the 1P frequency range of those instances simulated with low T.I. values and low imbalance fault degree measures. This reasoning makes sense because increasing magnitudes of T.I. masks certain signal dynamics associated with increasing pitch angle deviations of the rotor blades. Therefore, even if the pitch angle deviation of a rotor blade is large for one particular instance, if the T.I. associated with this instance is also large, the statistical nature of the features extracted are virtually indistinguishable from those coming form the instance simulated with both a low T.I. and low imbalance fault degree measure.

Lastly, when evaluating the performance of the MLR_{Phy}, KNN_{Phy}, and ANN_{Phy} models, which combine both current flow speed prior knowledge integration and T.I. physics-guided learning into their respective machine learning pipelines, the highest possible accuracy is attained through these approaches. The MLR_{Phy}, KNN_{Phy}, and ANN_{Phy} models in particular are able to perform T.I. classification when performing imbalance fault detection, for which the MLR_{Phy}, and KNN_{Phy} models attain a classification accuracy ranging between 86%–94%, while the ANN_{Phy} model achieves an accuracy ranging between 88%–98%. This improved accuracy is attributed to the fact that turbulence intensity classification is finally being performed through the implementation of the physics-guided loss function. As stated previously, shaft torque variations resulting from misaligned rotor blades induce varying dynamic loads and vibrations onto the turbine's rotor shaft. These varying dynamic loads and vibrations eventually manifesting themselves as frequency excitations within the 1P frequency range of $P_s(t)$. However, these manifestations can also be masked with increasing amounts of T.I. Therefore, having a means of reliably quantifying T.I. also allow the magnitude of the masking effect to be quantified by these models, thus ensuring better performance.

5.4. Computational costs analysis

The computational cost associated with the implementation of our proposed fault detection framework should be considered in two separate phases. The initial offline training phase consists of all of the hyper-parameter optimizations and machine learning training needed to properly calibrate our framework for fault detection and severity classification tasks. These calibrations include, but are not limited to wavelet hyper-parameter optimizations, wavelet coefficient thresholding, neural network L_1 and L_2 norm determination, etc. This initial phase occurs entirely offline, and took approximately 4.5 days to complete. However, this phase is something that only needs to be done once. The computational cost of the second phase is relatively low since all of the training, tuning, and thresholding has already been completed. New instances are simply projected onto the already established models in real time. The Tic-Toc function provided by MATLAB revealed that only 11.3356 s of elapsed time was needed to fully classify a new sample instance. These new instances can be processed as little or as frequently as needed, ranging from several times per hour to several times per month. For reference, a typical instance utilized in this research is a 50 s long generator power signal, sampled at a frequency of 200 Hz.

Lastly, it should be noted that our proposed framework does not require the use of complex sensor networks (e.g., ones containing vibration, strain, torque, acoustic emission sensors, etc.) that are currently used in contemporary fault detection and condition monitoring systems. Thus, when taken together, the relatively low computational costs of the second phase, coupled with the negation of an intrusive sensory network means that our proposed framework can be effortlessly integrated into existing OCT control systems.

Table 3
Study comparing the performance of state of the art frameworks proposed by Wei et al. (2021) and Freeman et al. (2021) against our newly proposed.

Test set comparative study (w/95% Confidence)			
Total number of Test Set Simulations: 720			
Error metric	Wei et.al.	Freeman et.al.	Our proposed
Accuracy (%)	59.03%	61.11%	92.08%
Phy-based Violations	N/A	N/A	57
Type II Error (%)	36.93%	44.64%	2.92%
Type I Error (%)	63.07%	55.36%	5.00%

5.5. Comparative study with other state-of-the-art approaches

Our proposed fault detection and severity classification algorithm was compared against the works done by Wei et al. in (Wei et al., 2021) and the previous work of Freeman et al. in (Freeman et al., 2021). For this comparative study, Wei's method was chosen in particular because it confronted challenges associated with performing imbalance fault detection on a variable speed rotor. In summary, Wei's algorithm begins first by using the HT to perform phase demodulation on the generator stator current signal of a MCT. Next, WMD is utilized to denoise the demodulated stator current signal before the application of power spectral density analysis (PSD). Lastly, screening linear discriminant analysis (S-LDA) is applied on the analyzed PSD signal for fault severity classification. The performance of the fault detection framework utilized by Wei was cited as being able to correctly predicted the presence and severity of a pitch imbalance fault 92.04% of the time.

In contrast, Freeman's framework in Freeman et al. (2021) begins by employing a Morlet CWT on the generator power signal of a MCT for demodulating purposes. Then, statistical features are extracted from the wavelet coefficients residing within the 1P frequency range of the signal. PCA is then employed on the wavelet coefficient feature space, where a K-Nearest Neighbor classifier is utilized to perform fault detection and severity classification. Results from Freeman's work demonstrated that the presence of a pitch imbalance fault can be accurately detected 100% of the time, and correctly classified based upon severity more than 97% of the time. Since the work performed in this study is an extension of Freeman's work in Freeman et al. (2021), it was important to also include this work in the comparative study.

Both methods were tested and compared against our proposed framework using the data set generated for this current work. This new data set is an extension of the data set used in Freeman et al. (2021), where in this new scenario, data was generated with a wider range of current flow speeds and T.I. values than what was included in either of works Wei et al. (2021) or Freeman et al. (2021). This new data set is intended to more closely resemble at sea conditions over an extended period of time, and therefore represents a more challenging OCT operating scenario. To the best of our knowledge, no other works investigate the effects of at sea conditions on the performance of OCTs as extensively as what was presented in our current work. Therefore, we are confident that the scientific merit and contribution of this work is worthwhile to all relevant research communities.

As depicted in Table 3, when Wei's framework (Wei et al., 2021) is employed on the new data set its performance dropped severely. In particular, once instances possessing different current velocities and T.I. were fed into the framework, the increased complexity of the $P_s(t)$ signal morphology caused the effectiveness of the S-LDA to diminish. As shown, Wei's method was only able to achieve an accuracy of 59.03%, for which of the total misclassifications present, 36.93% of them were

Table A.4
List of the most relevant parameters used in the development of framework.

Symbol	Description
J_R	Moment of Inertia
ω_R	Angular rotational speed of rotor
T_R	Hydrodynamic Torque induced on rotor
$T_\mathcal{E}$	Electromagnetic torque induced on rotor
T_τ	Hydrodynamic torque induced on rotor from turbulence
T_D	Deviation in torque from turbulence
ω_τ	Angular rotational speed of rotor in turbulence
ω_D	Angular speed deviation of rotor in turbulence
T_F	Hydrodynamic Torque induced on rotor under turbulence and imbalance fault conditions
ω_F	Angular rotational speed of rotor in turbulence and imbalance fault conditions
ω_I	Angular speed deviation induced on rotor from turbulence and imbalance fault conditions
A_v	Magnitude of shaft torque variation resulting from pitch imbalance fault conditions
$I_s(t)$	Generator stator current signal
I_F	Component of $I_s(t)$ from variable ocean current velocity and imbalance fault conditions
$f_s(t)$	Fundamental frequency of $I_s(t)$
A_i	Amplitude component of $I_s(t)$ stemming from imbalance fault
A_f	Amplitude component of f_F stemming from imbalance fault
φ_i	Phase component of $I_s(t)$ stemming from imbalance fault
φ_f	Phase component of $I_s(t)$ stemming from imbalance fault
f_R	Fundamental frequency of $I_s(t)$
$I_\mathcal{M}$	Modulated generator stator current signal
P	Three phase instantaneous power signal of the generator
V	Terminal voltage of the generator stator
$P_s(t)$	Single Phase power output by the generator
V_{LL}	Maximum supply line-to-line voltage
I_{sup}	Fundamental supply current
φ_s	Initial phase angle of the fundamental supply current
φ_F	Initial phase angle of I_{sup} when φ_s of f_F equals $f_s(t) + m \cdot f_R$
φ_{FN}	Initial phase angle of I_{sup} when φ_s of f_F equals $f_s(t) - m \cdot f_R$
m	Constant positive integer
I_{fault}	Peak value of $I_s(t)$ when f_F equals $f_s(t) + m \cdot f_R$
I_{FF}	Maximum value of $I_s(t)$ when f_F equals $f_s(t) - m \cdot f_R$
$\mathbf{U}$	Turbulence intensity time domain feature set and their associated labels
$\mathbf{F}_T$	Time domain features used to classify turbulence
$\mathbf{F}_S$	Time domain feature labels used to classify turbulence
Loss	Neural Network empirical loss function.
λ_{PB}	Physics-based hyper-parameter dictating importance of physics-based inconsistencies
$\mathbf{Loss}_{PHY}$	Physics-based loss term used by the framework's empirical loss function.
TI	Magnitude of simulated Turbulence Intensity
$\mathbf{TI}_{approx}$	Magnitude of Turbulence Intensity approximated by our framework
STD	Standard deviation operator

attributed to Type-II errors, with the remaining 63.07% of them corresponding to Type-I errors. Similarly, the performance of Freeman's previous framework also demonstrated unsatisfactory performance. In summary, the overall accuracy achieved was only slightly better at 61.11%, for which of the total misclassifications present, 44.64% of them were attributed to Type-II errors, with the remaining 55.36% of them corresponding to Type-I errors.

Our newly proposed framework was able to achieve an accuracy score of 92.08%, for which only 2.92% of the total instances classified were attributed to Type-II errors, and 5.00% of the total instances classified were attributed to Type-I errors. This improved performance is attributed to the T.I. classification that was performed by the physics-informed loss function that is integrated into our framework's machine learning pipeline. Furthermore, it should also be noted, that the 57 physics-based violations that were made by our framework can all be attributed to incorrect current flow speed classifications that were made in step 2 of Fig. 3, and not necessarily because of any inherent deficiencies with the physics-informed loss function. If Eq. (27) is referenced, then this finding makes sense, as the average current flow speed is a variable that needs to be known in order to calculate T.I. In contrast, neither of the frameworks developed by Wei or Freeman provided a means to classify T.I. (hence the reason of the N/A entries in Table 3). This implies that neither methods is capable of accounting for the masking of imbalance fault signatures within that coincides with increasing magnitudes of T.I. (see Figs. 10(a) and 10(c) and Section 5.1).

6. Conclusions

In this paper, we developed a novel fault detection and severity classification framework for OCT rotor blade imbalances. The robustness of the framework was enhanced through the integration of physics-based prior knowledge into the framework's machine learning pipeline. This prior knowledge was derived from oceanic environmental parameters acquired from a 13-month ADCP case study. Through the use of this prior knowledge, we engineered a never before used feature for rotor blade imbalance fault detection that approximated ambient T.I. We then used this feature to construct a physic-guided neural network, which in itself utilized a physics-based loss function to constrain T.I. predictions according to the turbine's underlining rotor dynamics. Our framework was able to achieve an average classification accuracy of 92.08%, while maintaining a 2.92% Type II and a 5.00% Type I error rate. These results compared favorably to other state of the art methods in this field, (Wei et al., 2021; Freeman et al., 2021), where only a respective 59.03% and 61.11% accuracy score was obtained using the data set created for this work. In the future, we hope to further expand the robustness of our framework via the incorporation of transfer-learning based fault detection approaches.

CRediT authorship contribution statement

Brittny Freeman: Conceptualization, Methodology, Writing – original draft. **Yufei Tang:** Supervision, Writing – review & editing. **Yu**

Huang: Experiments, Writing – review & editing. **James VanZwieten:** Data creation, Writing – review & editing.

Declaration of competing interest

The authors declare that they have no known competing financial interests or personal relationships that could have appeared to influence the work reported in this paper.

Acknowledgments

This work was supported in part by the U.S. National Science Foundation through Grant Nos. ECCS-1809164, CMMI-2145571, OAC-2017597 and the U.S. Department of Energy, Water Power Technologies Office, under Award No. DE-EE0008955.

Appendix

See Table A.4

References

Addison, Paul S., 2017. The Illustrated Wavelet Transform Handbook: Introductory Theory and Applications in Science, Engineering, Medicine and Finance. CRC Press.

Ali, Jaouher Ben, Saidi, Lotfi, Harrath, Salma, Bechhoefer, Eric, Benbouzid, Mohamed, 2018. Online automatic diagnosis of wind turbine bearings progressive degradations under real experimental conditions based on unsupervised machine learning. Appl. Acoust. 132, 167–181.

Chasnov, Jeffrey R., 1991. Simulation of the Kolmogorov inertial subrange using an improved subgrid model. Phys. Fluids A 3 (1), 188–200.

Cohen, Mike X., 2014. Analyzing Neural Time Series Data: Theory and Practice. MIT Press.

Cohen, Michael X., 2019. A better way to define and describe morlet wavelets for time-frequency analysis. NeuroImage 199, 81–86.

Freeman, Brittny, Tang, Yufei, Huang, Yu, VanZwieten, James, 2021. Rotor blade imbalance fault detection for variable-speed marine current turbines via generator power signal analysis. Ocean Eng. 223, 108666.

Gong, Xiang, Qiao, Wei, 2012. Imbalance fault detection of direct-drive wind turbines using generator current signals. IEEE Trans. Energy Convers. 27 (2), 468–476.

Gong, Xiang, Qiao, Wei, 2013. Bearing fault diagnosis for direct-drive wind turbines via current-demodulated signals. IEEE Trans. Ind. Electron. 60 (8), 3419–3428.

Karpatne, Anuj, Watkins, William, Read, Jordan, Kumar, Vipin, 2017. Physics-guided neural networks (pgnn): An application in lake temperature modeling. arXiv preprint arXiv:1710.11431.

Li, Yazhou, Dai, Wei, Zhang, Weifang, 2020a. Bearing fault feature selection method based on weighted multidimensional feature fusion. IEEE Access 8, 19008–19025. http://dx.doi.org/10.1109/ACCESS.2020.2967537.

Li, Zhichao, Wang, Tianzhen, Wang, Yide, Amirat, Yassine, Benbouzid, Mohamed, Diallo, Demba, 2020b. A wavelet threshold denoising-based imbalance fault detection method for marine current turbines. IEEE Access 8, 29815–29825.

Moon, Seung-Hyun, Kim, Yong-Hyuk, 2020. An improved forecast of precipitation type using correlation-based feature selection and multinomial logistic regression. Atmos. Res. 240, 104928.

Neary, Vincent Sinclair, Lawson, Michael, Previsic, Mirko, Copping, Andrea, Hallett, Kathleen C, LaBonte, Alison, Rieks, Jeff, Murray, Dianne, 2014. Methodology for Design and Economic Analysis of Marine Energy Conversion (MEC) Technologies. Technical Report, Sandia National Lab.(SNL-NM), Albuquerque, NM (United States).

Pyakurel, Parakram, VanZwieten, James H, Dhanak, Manhar, Xiros, Nikolaos I, 2017. Numerical modeling of turbulence and its effect on ocean current turbines. Int. J. Mar. Energy 17, 84–97.

Rai, Rahul, Sahu, Chandan K., 2020. Driven by data or derived through physics? a review of hybrid physics guided machine learning techniques with cyber-physical system (cps) focus. IEEE Access 8, 71050–71073.

Saidi, Lotfi, Benbouzid, Mohamed, Diallo, Demba, Amirat, Yassine, Elbouchikhi, Elhoussin, Wang, Tianzhen, 2020. Higher-order spectra analysis-based diagnosis method of blades biofouling in a PMSG driven tidal stream turbine. Energies 13 (11), 2888.

Tian, Wenlong, VanZwieten, James H, Pyakurel, Parakram, Li, Yanjun, 2016. Influences of yaw angle and turbulence intensity on the performance of a 20 kW in-stream hydrokinetic turbine. Energy 111, 104–116.

TSI, Precision Measurements Tools, 2012. Turbulence intensity measurement models: 9555, 9565, 7565, 7575, TA460, TA465, EBT730, PH730, 8715. Application Note TSI-141.

Tzelepis, Vasileios, VanZwieten, James H, Xiros, Nikolaos I, Sultan, Cornel, 2017. System modeling and simulation of in-stream hydrokinetic turbines for power management and control. J. Dyn. Syst. Meas. Control 139 (5).

VanZwieten, James H., Pyakurel, Parakram, Ngo, Tri, Sultan, Cornel, Xiros, Nikolaos I., 2016. An assessment of using variable blade pitch for moored ocean current turbine flight control. Int. J. Mar. Energy 13, 16–26. http://dx.doi.org/10.1016/j.ijome.2016.01.002, URL http://www.sciencedirect.com/science/article/pii/S2214166916000035.

VanZwieten, J.H., Vanrietvelde, N., Hacker, B.L., 2013. Numerical simulation of an experimental ocean current turbine. IEEE J. Ocean. Eng. 38 (1), 131–143. http://dx.doi.org/10.1109/JOE.2012.2218891.

von Rueden, Laura, Mayer, Sebastian, Beckh, Katharina, Georgiev, Bogdan, Giesselbach, Sven, Heese, Raoul, Kirsch, Birgit, Pfrommer, Julius, Pick, Annika, Ramamurthy, Rajkumar, et al., 2019. Informed machine learning–a taxonomy and survey of integrating knowledge into learning systems. arXiv preprint arXiv:1903.12394.

Watson, Simon Jonathan, Xiang, Beth J, Yang, Wenxian, Tavner, Peter J, Crabtree, Christopher J, 2010. Condition monitoring of the power output of wind turbine generators using wavelets. IEEE Trans. Energy Convers. 25 (3), 715–721.

Wei, Jiajia, Xie, Tao, Shi, Ming, He, Qianqian, Wang, Tianzhen, Amirat, Yassine, 2021. Imbalance fault classification based on VMD denoising and S-LDA for variable-speed marine current turbine. J. Mar. Sci. Eng. 9 (3), 248.

Yan, Ruqiang, Gao, Robert X., Chen, Xuefeng, 2014. Wavelets for fault diagnosis of rotary machines: A review with applications. Signal Process. 96, 1–15.

Zhang, Milu, Wang, Tianzhen, Tang, Tianhao, Benbouzid, Mohamed, Diallo, Demba, 2017. An imbalance fault detection method based on data normalization and EMD for marine current turbines. ISA Trans. 68, 302–312.